




The effect of heat treatment on the interface of 15–5 PH martensitic stainless steel and SAF 2507 duplex steel in functionally graded AM components

Martina Koukolíková^{1,*} , Pavel Podaný¹, Sylwia Rzepa¹, Michal Brázda¹, and Aleksandra Kocijan²

¹COMTES FHT a.s., Průmyslová 995, 334 41 Dobřany, Czech Republic

²Institute of Metals and Technology (IMT), Lepi pot 11, 1000 Ljubljana, Slovenia

Received: 22 March 2023

Accepted: 22 June 2023

Published online:
1 July 2023

© The Author(s), under exclusive licence to Springer Science+Business Media, LLC, part of Springer Nature 2023

ABSTRACT

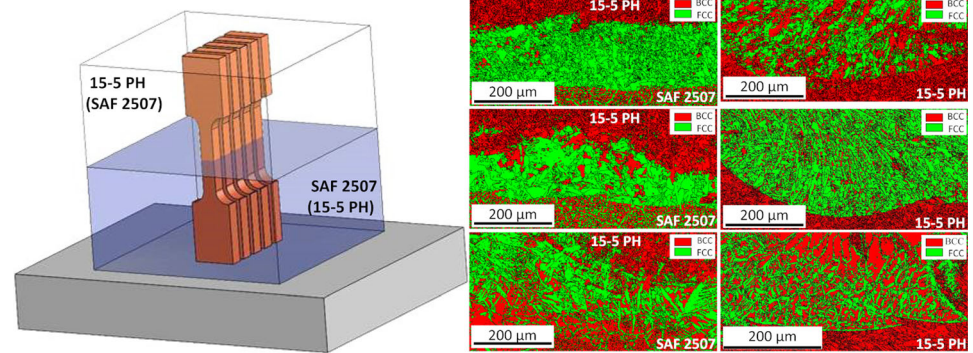
Multi-material components, also known as functionally graded materials (FGMs), are innovative materials that possess unique properties due to their composition and have many potential applications in engineering and science. The effect of the heat treatment (HT) of functionally graded materials 15–5 precipitation-hardened (PH) martensitic steel and SAF 2507 duplex stainless steel (and the opposite order of deposition, i.e. SAF 2507 first followed by 15–5 PH stainless steel) on the interface microstructures was systematically investigated in the presented research. The choice of HT followed the trend of optimum post-processing for the individual alloys. A significant modification in the interface microstructure, characterized in the microstructural transition zone (MTZ) formed above the fusion line. Mechanical properties by miniaturized testing method including hardness measurement characterized both types of interfaces. The sequence of the materials' application did not have a significant effect on their final mechanical tensile properties in the heat-treated states. Nevertheless, the microstructural change at the MTZ led to drop in the hardness at the interface. The research presents heat-treated FGMs in a horizontal configuration to form a high-quality metallurgical joint between heterogeneous materials manufactured by powder-based directed energy deposition method.

Handling Editor: Sophie Primig.

Address correspondence to E-mail: martina.koukolikova@comtesfht.cz

<https://doi.org/10.1007/s10853-023-08718-7>

GRAPHICAL ABSTRACT



Introduction

Functionally graded materials (FGMs) are a class of advanced materials that exhibit either sharp or gradual variation in composition and microstructure over their volume. This unique characteristic allows FGMs to possess tailored properties, making them ideal for a wide range of applications. The FGM materials were first produced more than 30 years ago and their development, coupled with additive manufacturing (AM), has increased significantly in the last few years. The researchers have investigated the material combination of nickel-based superalloys, cobalt, titanium alloys, and steels with either continuous or layered gradient interfaces produced by various deposition methods [1–7]. The FGM material investigated in this study represents a combination of 15–5 PH martensitic stainless steel and SAF2507 duplex steel, which has not been extensively investigated thus far. In most cases, these materials have been studied separately both in the as-built and post heat-treated states [8–12]. Precipitation-hardened 15–5 PH, a frequently used PH stainless steel in AM research, exhibits excellent high strength and corrosion resistance [13]. A low carbon lath martensite (α') with a body centred cubic (BCC) lattice is formed by these type of steels [14].

Duplex steel (DSS) is a type of stainless steel that consists of both austenitic and ferritic microstructures. DSSs offer a unique combination of high strength and corrosion resistance, realized by

chemical composition and microstructural balance, which makes them a popular material for various industrial applications. However, to achieve its full potential, duplex steel needs to undergo a heat treatment process. If not done correctly, the steel may experience reduced strength, corrosion resistance, and toughness in particular in the temperature interval 650–950 °C due to the formation of intermetallic secondary phases, such as σ phase, χ phase, chromium nitrides, carbides leading to harmful effect [15]. It is essential to follow the appropriate heat treatment specifications for each type of duplex steel, as the optimal parameters can vary based on factors such as composition and intended application. These stainless grades are used in many applications in the chemical, petrochemical, marine, energy, and offshore industries. The synergy achieved by combining SAF 2507 and 15–5 PH in an FGM offers the opportunity to tailor the material's properties according to specific application requirements. Both materials exhibit good corrosion resistance. However, the enhanced corrosion resistance of SAF 2507 can be beneficial in environments where corrosion is a concern, while the increased strength and wear resistance of 15–5 PH provide advantageous properties in applications requiring high mechanical strength. Numerous studies have reported that 15–5 PH demonstrates a significantly higher ultimate tensile strength (UTS) and yield strength (YS) compared to SAF 2507, with an approximate difference of 40–50% [9, 11–13]. In mechanically stressed components such as valves, heat exchanger tubes, impellers, shafts,

rotors, vessels, offshore structures, pumps, the structural element support profile, made of 15–5 PH, would provide the necessary mechanical strength, while the functional surface in contact with corrosive mediums would be composed of a material with superior corrosion resistance, such as duplex steel SAF 2507.

A microstructure consisting of almost equal proportions of ferrite (α) and austenite (γ) is produced by solution annealing of SAF 2507 at temperature interval 1020–1110 °C/1 h, followed by water quenching (WQ) [16, 17]. Heat treatment of 15–5 PH steel usually involves solution annealing heat treatment typically at 1040 °C for 1 h, followed by water quenching. The resulting martensitic microstructure is supersaturated in Cu. The following thermal ageing treatment induces a precipitation of Cu-rich precipitates and their growth in the BCC matrix [18]. The most commonly applied ageing treatment to 15–5 PH is reported in interval 480–620 °C for 1–4 h depending upon the temperature. The highest strength is achieved at 480 °C, referred as the H900 condition, where the kinetics of Cu precipitation results in peak age hardening [13, 18].

Duplex and PH stainless steels' good weldability by conventional welding processes such as tungsten inert gas (TIG) welding, electron beam welding, and laser beam has been demonstrated by various researchers [12, 16, 19–21]. Nevertheless, the production of FGM would be highly problematic if only conventional technologies were used. Since specific tailored chemical composition, microstructure, and mechanical properties of newly designed FGMs are required in manufacturing, the production of customized gradient components demands a new approach that has the flexibility to incorporate and mix multiple metallic elements. However, additive manufacturing, also known as 3D printing, has emerged as a promising technology. With AM, the production process is much easier, as the combination of materials in the form of powder and the possibility of changing the material composition where needed are favoured. Recently, the development of AM technologies has also enabled the production of complex geometries of multi-material components with optimized mechanical properties [22–24]. The selection of the method depends on the material system, the desired properties, and the application requirements.

Powder-based directed energy deposition (DED) technology equipped with separate feeders enables the powders to be fed simultaneously to the nozzle. This mixture is subsequently melted by the effect of the laser beam creating the desired FGMs. The thickness of the layer varies from 250 to 900 μm for DED, compared to 30 to 50 μm for L-PBF [23]. A specific feature of multi-material systems is the application of the adequate heat treatment, which will be optimal for both material groups. The heat treatment of functionally graded materials consisting of SAF 2507 with 15–5 PH is a crucial process that significantly affects the properties and performance of the material. The synergy of the properties of each material is advantageous for different combinations of materials. Therefore, the choice of heat treatment in this study follows the trend of optimum post-processing for the individual materials, i.e. 15–5 PH and SAF 2507. Solution treatment, as the first stage, ensured maximum concentration of solute dissolution within the matrix for both materials. Mechanical properties of 15–5 PH were improved by the formation of strengthening Cu precipitates during ageing without precipitation of undesirable phases in the duplex steel SAF 2507. A promising application of a heat-treated heterogeneous material combination of 15–5 PH martensitic steel and SAF 2507 duplex stainless steel in a horizontal configuration is explored in the presented manuscript. The research presented in this manuscript investigates the influence of applied heat treatment on the quality of individual interfaces, mechanical properties and the microstructural features of FGM blocks of 15–5 PH/SAF 2507. Light (LM) and electron microscopies (SEM), supplemented by grain, phase and texture characterization provided deep insight into the microstructure of the FGMs. The tensile test characteristics of the material were measured using a miniaturized specimen testing method. The novelty of the present study involves the heat treatment of AM heterogeneous multi-materials to combine the advantage of the best properties of both duplex SAF 2507 and martensitic 15–5 PH stainless steels, which is attributed to their superior metallurgical bonding. The use of SAF 2507 and 15–5 PH in an FGM has not been reported before. This study is the first to investigate the use of these two materials in combination to produce an FGM. This novelty can lead to the development of new materials with unique properties with optimized performance for specific

applications. FGM can exhibit both high corrosion resistance and high strength and toughness, making it suitable for a wide range of applications in offshore oil, gas production equipment, aerospace and aviation industries, and chemical processing equipment.

Materials and methods

The material blocks (Fig. 1) were produced by an INNSTEK MX-600 (InssTek, Daejeon, Korea) instrumented with a 2 kW yttrium fibre laser in an atmosphere of argon 5.0 (Air Products and Chemicals, Inc.) with purity 99.999%. The dimensions of the deposited FGM material samples were $15 \times 15 \times 15 \text{ mm}^3$. The deposited layers had a height of $250 \mu\text{m}$, a width of $800 \mu\text{m}$, and a hatch distance of $500 \mu\text{m}$. The feedstock used was nitrogen gas atomised powder from Sandvik Osprey Ltd. The average particle size was reported by the manufacturer to be $53\text{--}150 \mu\text{m}$ for 15-5 PH and $45\text{--}150 \mu\text{m}$ for SAF 2507. Table 1 presents the chemical composition of the powders as supplied by the manufacturer. Separate feeders fed the powders to the nozzle. A C45 platform was used to deposit the first layer of either 15-5 PH or SAF 2507. The DED process involved the deposition of two materials (15-5 PH and SAF 2507) to form two distinct interfaces by deposition of 15-5PH on SAF 2507 and vice versa. In each case, one material was deposited to the platform to a height of 7.5 mm , followed by the second material. The steel 15-5 PH (Sandvik Osprey Ltd., Sandviken, Sweden, lot: 20D0209) and SAF 2507 (Sandvik Osprey Ltd., Sandviken, Sweden, lot: 20D0211) were deposited in

a horizontal configuration using the Direct Metal Tooling (DMT) in the laser power range of $290\text{--}630 \text{ W}$. In DMT mode, the laser power is adjusted to retain a continuous layer at a distance of approximately 9 mm from the nozzle. The power is automatically reduced if the distance decreases and vice versa. A zigzag scanning approach with a 90° rotation of the layers was used with the SDM 800 module. Process parameters are summarized in Table 2. Miniaturized testing method (MTT) specimens (Fig. 1a) were produced via a wire electrical discharge machining and each condition was tested with three replicates.

The FGMs' microstructures were observed in the YZ plane parallel to the deposition direction Z. Metallographic preparation involved conventional grinding and subsequent polishing on a Struer's Tegramin 30. Beraha II etchant with potassium disulphide $\text{K}_2\text{S}_2\text{O}_5$ exposed SAF 2507 microstructure (ferrite is coloured dark, austenite remnants light), whereas Villela–Bain agent was used for the martensitic stainless steel etching. Light microscopy (LM) observations were performed on Nikon Eclipse MA200 with NIS Elements 5.2 digital image software. Detailed microstructural observations supported with energy dispersive spectroscopy (EDS—Octane Elite Super) and electron backscatter diffraction (EBSD) were performed on a JEOL IT 500 HR scanning electron microscope with an EDAX Hikari Super camera. EBSD maps were processed at $200 \times$ magnification with a step size of $0.5 \mu\text{m}$, analysed area $640 \times 500 \mu\text{m}^2$, acceleration voltage 20 kV , scanning speed $50\text{--}100$ points per second, and 5×5 binning. The data acquisition, analyses, and post-processing

Figure 1 Experiment details: **a** MTT specimen geometry; **b** FGM block.

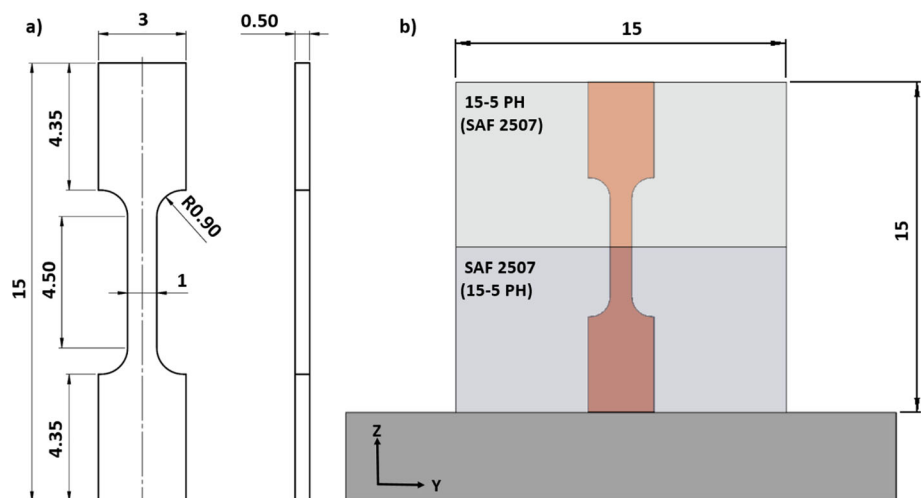


Table 1 Chemical composition of powders used in the DED process (in weight %)

Material	C	Mn	Si	Cr	Mo	Ni	Cu	Al	Nb	N	Fe
15 – 5PH	0.07	1.00	1.00	14.50–15.50	–	3.50–5.50	2.50–4.50	–	0.15–0.45		Bal
SAF2507	0.02	0.7–1.1	0.20–0.60	24.60–25.40	3.76–4.24	6.80–7.20	Max. 0.2	0.01		0.26–0.31	Bal

Table 2 Parameters of DED process

Laser spot size [μm]	Laser scanning speed [mm/min]	Powder feed rate [g/min]	Powder gas [l/min]	Shielding gas [l/min]	Coaxial gas [l/min]	Z step [mm]	Hatch distance [mm]
800	849	2.8	3	5	10	0.25	0.5

were performed using the software TEAM 4.5 and EDAX OIM AnalysisTM.

The suitable heat treatment, optimal for both material groups, without the undesirable phases' precipitation, was selected on the basis of an extensive literature search work by the authors. The solution annealing (SA) was performed in the experiment primarily due to the optimum corrosion resistance of duplex steel, achieved by almost 1:1 microstructure (ferrite: austenite) [16, 17]. SA is usually applied prior the precipitation hardening of 15–5 PH. As mentioned in the Introduction chapter, the SA temperature range is similar for both materials; therefore, a temperature of 1040 °C for one hour followed by WQ was selected. As the precipitation hardening at 480–620 °C for 1 h is reported as the most commonly used heat treatment of 15–5 PH and the highest level of strength is achieved at 480 °C temperatures, these temperatures and dwell times were applied accordingly. In order to see the behaviour of the materials also without SA application, the direct ageing regimes were selected at temperatures of 480 °C and 620 °C only. Table 3 summarizes a detailed specification of the selected heat treatment of FGM deposits. The interface I-SAF 2507_15-5 PH (material at the platform SAF 2507) and interface II characterizes

material combination 15–5 PH_SAF 2507 (material at the platform 15–5 PH). The focus of metallographic analyses and mechanical property testing in this research was dedicated on the interfaces of the FGMs in both variants.

The MTT testing was performed according to standard ISO 6892–1/ASTM E8 with a Tira Test universal testing machine fitted with a 10 kN load cell capacity. The samples were tested at a strain rate of 0.00025 s⁻¹ (A222) at room temperature under quasi-static conditions. A micrometre was used to measure the initial dimensions of the samples. The black-and-white pattern applied to the samples prior the testing enabled the deformation recording with a noncontact Mercury RT system, functioning on the principle of digital image correlation (DIC). The Young's modulus (E), the yield strength (YS), the ultimate tensile strength (UTS), the uniform elongation (UE), the total plastic elongation (El), and the reduction of area (RA) were evaluated using the recorded force–displacement records. This type of tests has already proved to be effective in previous studies [2, 12, 15].

Table 3 Heat treatment regimes with sample marking

Interface I	Interface II	Heat treatment
I_SA	II_SA	SA 1040 °C/ 1 h / WQ
I_SA_480	II_SA_480	SA 1040 °C/ 1 h / WQ / PH 480 °C / 1 h/ WQ
I_SA_620	II_SA_620	SA 1040 °C/ 1 h / WQ / PH 620 °C / 1 h/ WQ
I_480	II_480	PH 480 °C—1 h / WQ
I_620	II_620	PH 620 °C—1 h / WQ

Results

Functionally graded materials are multiple materials with spatial variations in their composition and microstructure. Heat treatment is used to modify the properties of FGMs by changing the composition and microstructure of the material. By controlling the temperature, time, and cooling rate, the microstructure and properties of the material have to be tailored to meet specific requirements for various applications. Since duplex stainless steel SAF 2507 achieves optimum corrosion resistance in the solution annealed condition [16, 17], material 15–5 PH dominates its properties after heat treatment referred as H900 [13, 18]. Therefore, photo documentation from metallographic analysis by light and electron microscopy, including EBSD, in combination with this heat treatment will be mainly presented in the study. The existence of Cu precipitates resulting from PH heat treatments, specifically H900 and H1150, has been well documented in studies [13, 14, 18]. However, the investigation of these precipitates was not the primary objective of the present research; therefore, their further analysis was not conducted. The results of three different heat treatment regimes, namely solution annealing, solution annealing with precipitation hardening, and direct precipitation hardening (as presented in Table 3) in each case with final water quenching, provided documentation of the FGMs' microstructural features and mechanical properties.

Microstructural features

In the present study, the solution annealing process applied to SAF 2507 steel resulted in a microstructure with ferrite content of 46% and austenite content of 54% (determined through EBSD analysis), which closely matched the microstructural features specified by the steel manufacturer [17]. A duplex microstructure of the SAF 2507, etched by the Beraha II etchant with potassium disulphide $K_2S_2O_5$, revealed microstructure with a ferritic matrix (dark) and austenite (light).

The evolution of the microstructure in the interfacial region, marked by a yellow dashed line in Fig. 2, was firstly analysed by light microscopy. After the as-built (AB) microstructure was characterized (Fig. 2a, c), the FGM was subjected to the heat treatments to investigate their impact on the microstructure. In the case of 15–5 PH etched by Villela–Bain, the lath

martensite dominated the microstructure. The interface consisted of a mixture of different types of austenite, including grain boundary austenite (GBA), Widmanstätten austenite (WA), and intragranular austenite (IGA) in ferritic matrix. SAF 2507 region dominated ferritic matrix with GBA, WA, and IGA with much lower fraction of austenitic phase. First approach to the heat treatment of FGMs was to use a solution annealing process. As can be evident from the LM images, this heat treatment led to the formation of a band of austenite at the interface I (Fig. 2b). Such a significant proportion of austenite was not achieved at the interface II (Fig. 2f). Subsequent PH led to a relatively high austenite fractions in the resulting microstructure in the interface regions of both types (Fig. 2c, g), especially when compared to the SA-free condition (Fig. 2d, h). The resulting microstructure of the interface after the direct PH process exhibited similar features as in the as-built state and this HT did not change the proportion of ferrite and austenite in the microstructure. No intermetallic secondary phases, such as σ phase, χ phase were observed neither by LM or SEM microscopy.

EBSD, a powerful technique used for microstructural analysis of materials, has proven to be a valuable tool for studying the microstructure and crystallographic orientation of FGMs [26, 27]. The crystallography is a crucial aspect in understanding the behaviour and properties of functionally graded materials. The orientation of the grains can influence the mechanical properties of the material, including the strength and ductility. It is essential to have a high degree of crystallographic compatibility between the two materials to minimize the interfacial stress and to prevent any interfacial defects from their forming. Figures 3 and 4 provide the inverse pole figure (IPF) maps of the various FGMs material combinations after heat treatment. No preferential grain growth was observed neither at interface I or interface II (highlighted by black dashed lines). Newly formed grains maintained the same crystallographic orientation and size as the original grains, which preserved the continuous grain boundaries across the fusion zone. This is particularly noticeable in Fig. 4a and samples after direct PH (Fig. 3d, e). The crystallographic orientation of the grains did not show any systematic alignment or preference in a particular direction. Texture intensities of ferrite (BCC) and austenite (FCC) grains at the interfaces

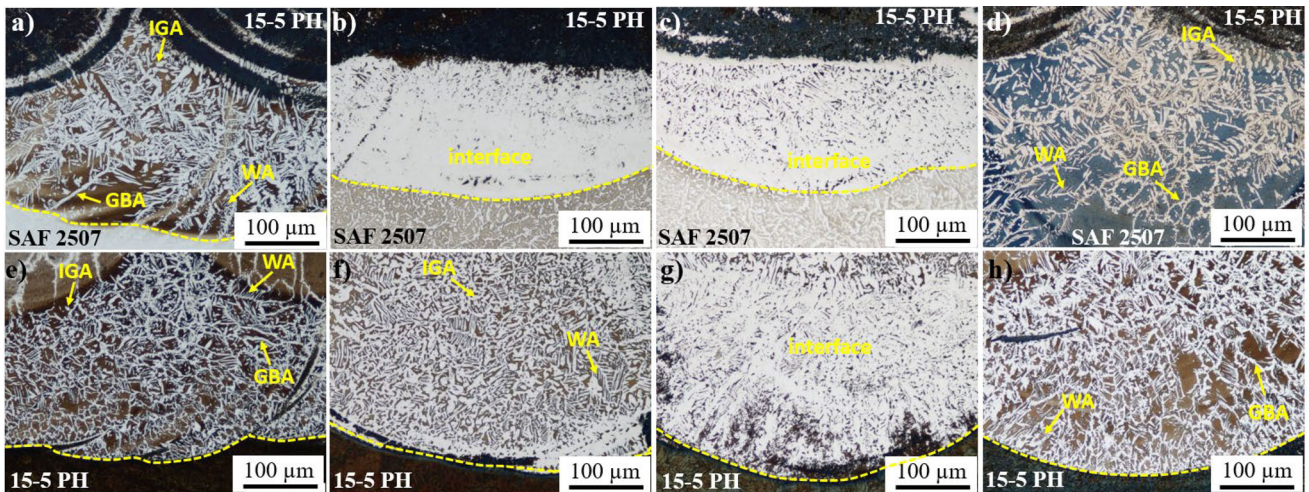


Figure 2 Observation of the sample interfaces' region by light microscopy: **a** interface I_AB; **b** interface I_SA; **c** interface I_SA_480; **d** interface I_480; **e** interface II_AB; **f** interface II_SA; **g** interface II_SA_480; **h** interface II_480.

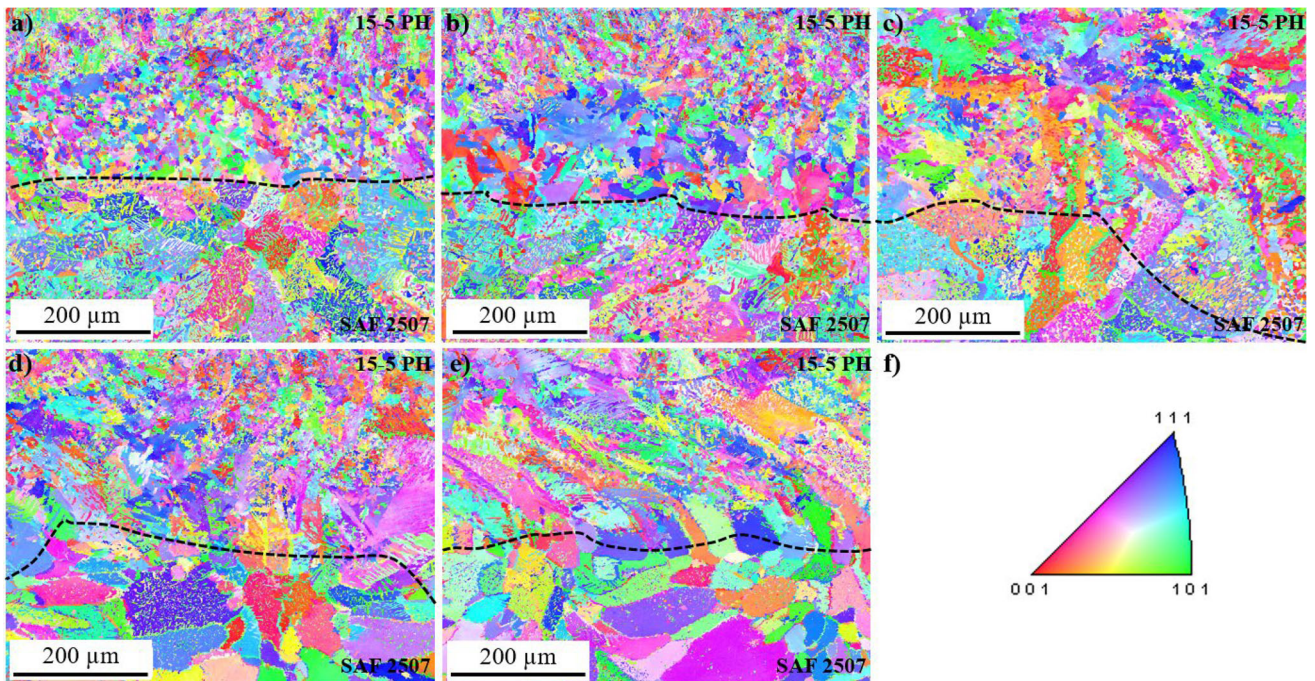


Figure 3 EBSD inverse pole figure maps: **a** interface I_SA; **b** interface I_SA_480; **c** interface I_SA_620; **d** interface I_480; **e** interface I_620; **f** IPF colour key.

reached maximum values for interface I-BCC 2.2 (sample I_SA_480), FCC 2.8 (sample I_480); interface II-BCC 3.6 (sample II_SA) and FCC 1.8 (sample II_480); therefore, the orientation of grains appears to be rather random, exhibiting low texture intensities. This could be due to several factors, such as the melting and solidification conditions, the composition of the material or the processing parameters and heat treatment process. However, an interesting

aspect to observe was that the sequence of the materials influenced the grains size and shape of the interface. In the case of 15–5 PH deposited on duplex steel, the SA conditions resulted in the formation of fine-grained FGM, while in the opposite direction, the SAF 2507 grains onto martensitic steel followed the direction of maximum thermal gradient involving columnar grain growth.

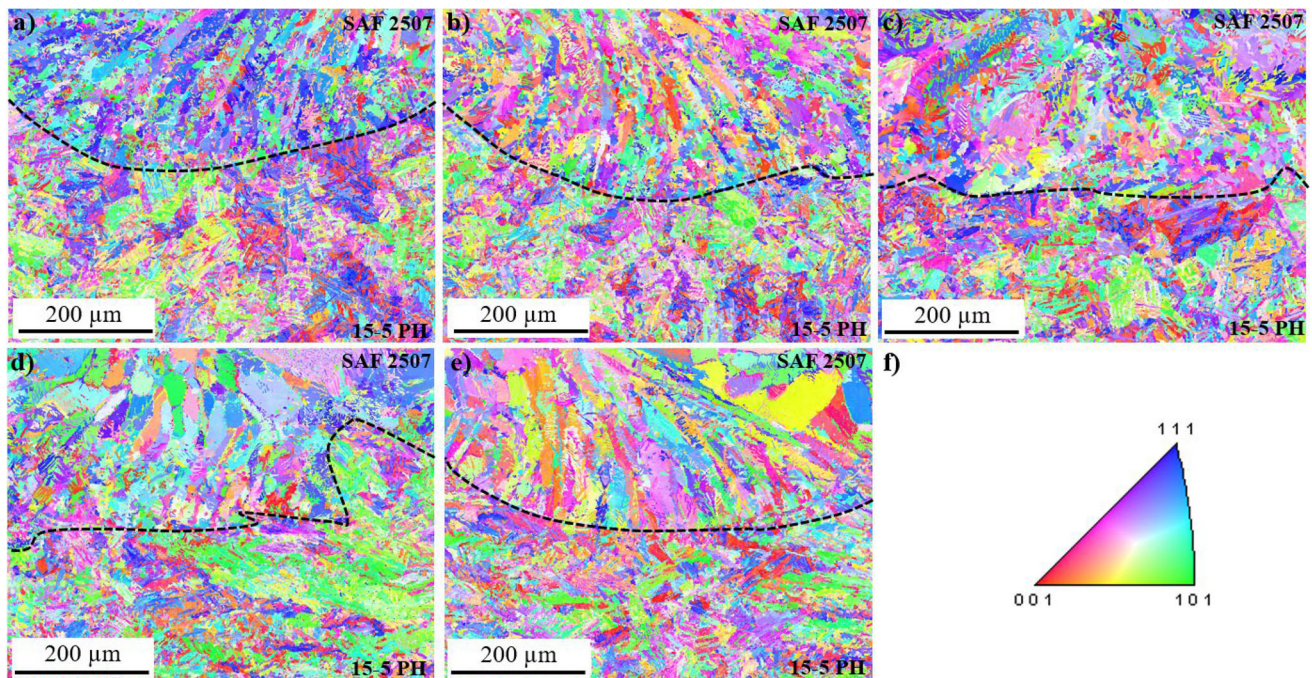


Figure 4 EBSD inverse pole figure maps: **a** interface II_SA; **b** interface II_SA_480; **c** interface II_SA_620; **d** interface II_480; **e** interface II_620; **f** IPF colour key.

Table 4 EDS results of the FGM samples I_SA_480 and II_SA_480

Element/Sample [wt %]	I_SA_480			II_SA_480		
	15-5 PH	Interface I	SAF 2507	15-5 PH	Interface II	SAF 2507
Si	0.5	0.5	0.5	0.5	0.5	0.4
Mo	0.0	1.8	3.9	0.0	1.7	3.6
Nb	0.3	0.0	0.0	0.2	0.1	0.0
Cr	16.2	21.0	27.1	16.3	21.0	27.1
Ni	4.2	5.4	6.5	4.0	5.2	6.5
Cu	5.1	1.9	0.1	4.8	1.9	0.2
Fe	Bal	Bal	Bal	Bal	Bal	Bal

The core of the problem is concerned with forming ferritic and austenitic phases at the two types of interfaces. The extent of the materials' mixing and distribution of elements across the interfaces, determined by the EDS analysis, reported the results in Table 4. The results proved mainly the Cu, Mo, Cr, and Ni content provide the element diffusion of materials in the microstructural transition zone (MTZ), as the resulting chemical composition lies within their original alloy composition.

Mechanical properties

Combining hardness measurements with microstructural characterization can provide a comprehensive understanding of the properties and

Table 5 Results of the HV5 hardness testing

HT/sample	15-5 PH	SAF 2507	Interface I	Interface II
AB	369 ± 9	303 ± 8	281 ± 6	279 ± 4
SA	324 ± 3	275 ± 5	232 ± 9	235 ± 3
SA_480	430 ± 4	306 ± 4	240 ± 8	252 ± 10
SA_620	329 ± 2	271 ± 4	232 ± 4	229 ± 15
480	464 ± 12	334 ± 7	269 ± 7	295 ± 13
620	370 ± 4	300 ± 6	265 ± 9	280 ± 9

performance of multicomponent materials. Hardness measurements (Table 5) in both interface regions and the individual alloys provided important information about the mechanical properties of a multicomponent

material. The performed SA with the achieved proportions of ferrite (46%) and austenite (54%) reached the hardness values declared by the manufacturer of SAF 2507 steel produced by L-PBF [17]. The hardness in the interface regions was found to be lower than in the individual alloys' hardness for all heat-treated states. This could potentially compromise the mechanical integrity of the material. The solution annealing applied prior to the heat treatment led to the slight decrease in the final hardness values of the interfaces, SAF 2507 and 15–5 PH alloys.

The hardness reached similar values at the interface region I and the interface region II for states, as-built (AB), SA and I_SA_480, so the sequence of materials has not significantly affected the mechanical properties of the FGM material from the hardness point of view. For the higher PH temperatures and SA-free states (samples SA_620, I_480, II_620), the resulting interface I hardness is slightly lower.

The gradual decrease in 15–5 PH hardness (Table 5), YS and UTS (Table 6) beyond the peak limit reached at 480 °C ageing temperature was in accordance with Peng et al. [18]. Peng reported that the mechanical properties of a material decreased at an ageing temperature interval 550–620 °C. This decrease in mechanical properties was attributed to the weakening effect caused by the coarsening of Cu precipitates, which was greater than the strengthening effect caused by the precipitation.

The results of elastic modulus measurement are graphically summarized in Fig. 5a. For both interfaces, the lowest values of elastic modulus were recorded for the materials subjected to solution annealing with subsequent water quenching (samples I_SA and II_SA). This mechanical property yielded the average value slightly below 150 GPa.

The highest values were observed in the case of the materials after SA, PH, and water quenching (samples I_SA_480, II_SA_480) as well as PH and water quenching, i.e. batches designated as samples I_480, II_480. The materials in SA, PH + water quenched (I_SA_620, II_SA_620), and PH + water quenched (I_620, II_620) states were characterized by average elastic modulus values above 150 GPa. Summarized results (Fig. 5) of mechanical behaviour of FGMs under different conditions analysed by MTT for a PH material typically exhibited a higher yield strength (Fig. 5b) and a lower elongation (Fig. 5d) compared to the SA state, indicating higher strength (Fig. 5c) and reduced ductility.

The average values obtained from MTT testing (3 tested samples) are summarized in Table 6. Since in practice these stainless steels are used in the solution annealed (SAF 2507) and precipitation-hardened (SA + PH at 480 °C) conditions, where 15–5 PH reaches its peak hardness, the resulting mechanical properties of the SA_480 heat treatment were of the highest interest for both interfaces measured (samples I_SA_480, II_SA_480). The achieved values follow the expected trend of the evolution of especially YS, UTS, and El.

The interface I (sample I_SA_480) reached YS 623 MPa, UTS 873 MPa with 13% elongation, whereas the interface II (sample II_SA_480) reached YS 603 MPa, UTS 840 MPa with 15% elongation. In the case of both kinds of interfaces, the materials in SA state (samples I_SA and II_SA) were distinguished by lower values of YS and UTS (about 550 and 800 MPa, respectively) in comparison to the only PH/WQ materials. The use of SA, both as a standalone heat treatment and in combination with PH, had a significant influence on the resulting

Table 6 Results of the mechanical testing MTT

Specimen	E GPa	YS MPa	UTS MPa	UE %	El %	RA %
I_SA	149 ± 8	556 ± 8	807 ± 10	14 ± 1	21 ± 1	67 ± 3
II_SA	150 ± 1	586 ± 10	794 ± 7	11 ± 0	19 ± 1	74 ± 1
I_SA_480	160 ± 3	623 ± 6	873 ± 2	8 ± 0	13 ± 1	64 ± 3
II_SA_480	155 ± 3	603 ± 14	840 ± 20	9 ± 0	15 ± 1	82 ± 4
I_SA_620	151 ± 9	569 ± 5	811 ± 4	12 ± 0	20 ± 1	77 ± 3
II_SA_620	152 ± 5	575 ± 16	804 ± 3	11 ± 0	20 ± 1	80 ± 0
I_480	158 ± 1	753 ± 26	958 ± 12	7 ± 1	12 ± 2	75 ± 1
II_480	157 ± 2	779 ± 23	919 ± 22	5 ± 1	10 ± 2	63 ± 2
I_620	151 ± 8	655 ± 18	892 ± 7	9 ± 0	16 ± 1	66 ± 5
II_620	153 ± 2	678 ± 5	869 ± 5	6 ± 0	12 ± 1	68 ± 3

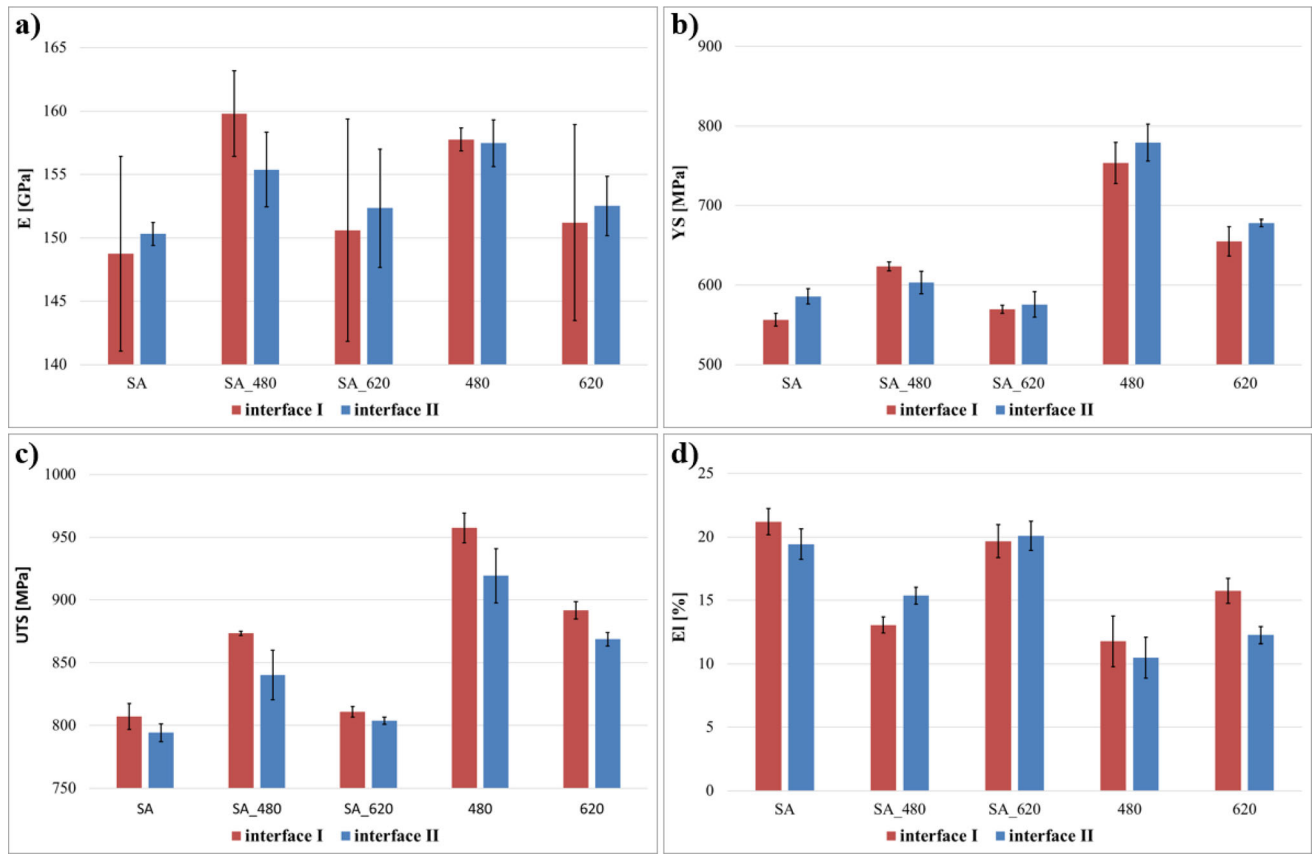


Figure 5 Miniaturized tensile test results: **a** Young's modulus values; **b** yield strength; **c** ultimate tensile strength; **d** elongation.

mechanical properties, making it a crucial factor to consider from a mechanical property perspective. The influence of SA particularly affected the microstructure of SAF 2507, whereas the subsequent precipitation hardening (PH) had a relatively minimal impact on its microstructure and associated mechanical properties. However, PH had a dominant effect on the properties of 15–5 PH and played a dominant role in determining the behaviour of the FGM as a whole. By reaching the peak hardness at 480 °C for 15–5 PH due to the formation of Cu precipitates [13, 18], there was a significant increase in the strength of the FGM part on the 15–5 PH side, leading to predominant deformation occurring in the region of the duplex steel. Therefore, PH materials extracted from both interfaces reached higher strength, while the highest values (above 900 MPa) were recorded for the specimens directly aged at 480 °C (samples I_480 and II_480); however, high strength was accompanied by reduced elongation values. The lowest elongation, which reached a value slightly higher than 10%, was observed in the case of

the specimens directly aged at 480 °C for both kinds of interface (samples I_480 and II_480). The elevated direct ageing temperature of 620 °C (samples I_620, II_620) resulted in decreased hardness, attributed to Cu coarsening in the case of 15–5 PH [18], and increased annealing of SAF 2507. In the context of the FGM as a whole, these factors contribute to a reduction in hardness, yield strength (YS), and ultimate tensile strength (UTS) values. The materials subjected to solution annealing and solution annealing with PH at 620 °C (samples I_SA, II_SA, I_SA_620, II_SA_620) were characterized by the highest elongation (about 20%) regardless the order of material deposition. The values of strength and elongation evaluated for all experimental materials are characterized by a relatively low standard deviation, which indicates high repeatability of the results obtained using miniaturized specimens. The fractographic analysis presented at the end of the chapter further confirmed the predominant deformation occurring in the region of the duplex steel.

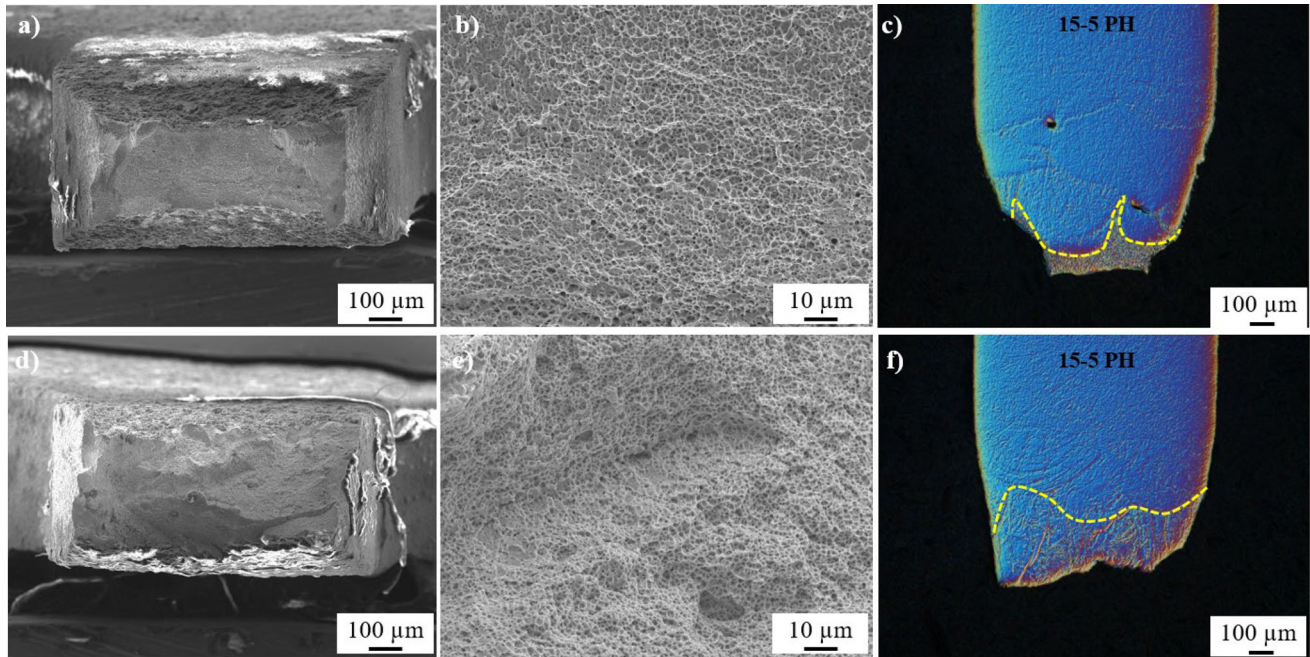


Figure 6 SEM fractography of MTT specimens: **a** overview images of the fracture surface-I_SA_480; **b** transcrystalline ductile fracture-I_SA_480; **c** DIC light microscopy section-I_SA_480; **d** overview images of the fracture surfaces-I_480; **e** transcrystalline ductile fracture-I_480; **f** DIC light microscopy section-I_480.

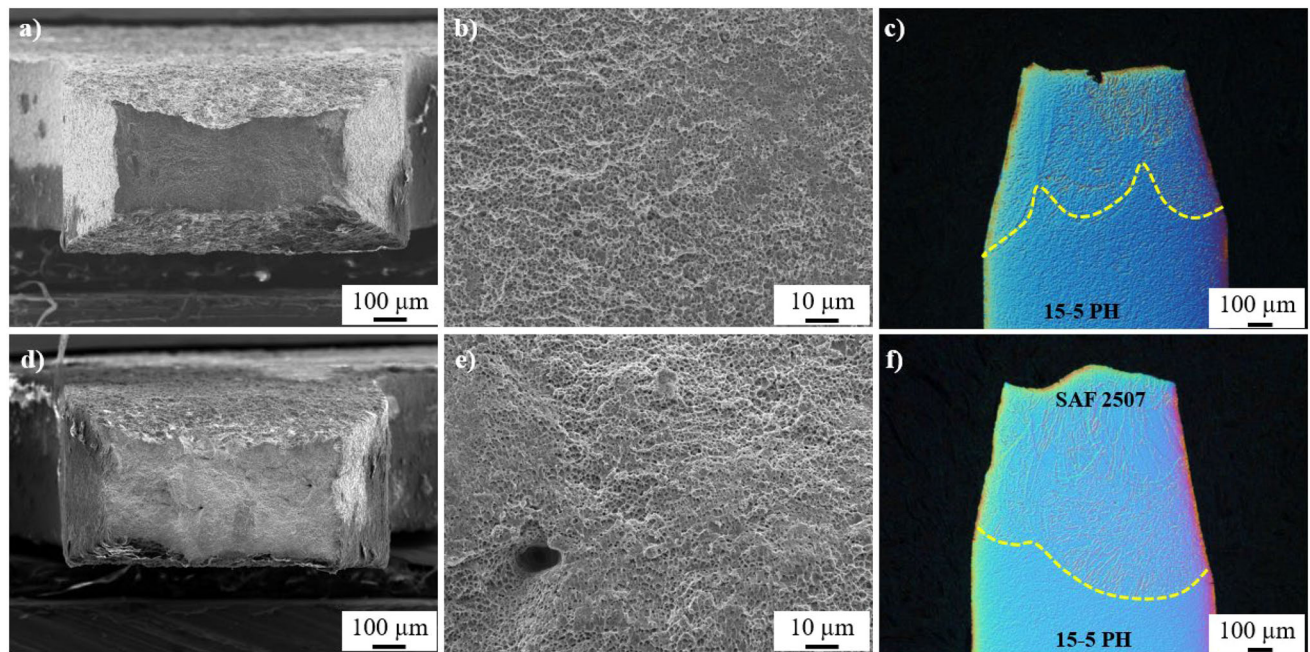


Figure 7 SEM fractography of MTT specimens: **a** overview images of the fracture surface-II_SA_480; **b** transcrystalline ductile fracture-II_SA_480; **c** DIC light microscopy section-II_SA_480; **d** overview images of the fracture surfaces-II_480; **e** transcrystalline ductile fracture with presence of pore-II_480; **f** DIC light microscopy section-II_480.

The location of the fracture surfaces can provide an important information about the FGMs mechanical properties and behaviour under load. The fracture

surfaces (Figs. 6 a, d and 7 a, d) were analysed by SEM to observe the morphology and to identify the fracture mode. Cases of transcrystalline ductile

Table 7 Fractography of representative MTT specimens with evaluated fracture location

Sample	Location of the fracture	Sample	Location of the fracture
I_SA	Interface	II_SA	SAF 2507
I_SA_480	SAF 2507	II_SA_480	Interface
I_SA_620	SAF 2507	II_SA_620	SAF 2507
I_480	SAF 2507	II_480	SAF 2507
I_620	SAF 2507	II_620	SAF 2507

fracture with dimpled morphology (Figs. 6 b, e and 7 b, e) were observed for all specimens. The fractures were predominantly located in the SAF 2507 region, which was observed for both types of interfaces (Table 7). Only exceptional cases have proved the appearance of fracture in the interface area. The morphology and fracture localization for selected samples I_SA_480 (Fig. 6) and II_SA_480 (Fig. 7) document the failure of FGMs after MTT testing. The yellow dashed line on the optical microscopy images (Figs. 6 c, f and 7 f) with differential interference contrast (DIC) indicate the interface. The fractographic analysis did not prove that defects from the AM process, i.e. pore or lack of fusion, initiated failure at the fracture surfaces.

Discussion

The choice of FGMs plays a significant role in the development of new and innovative materials that effectively address the current challenges in diverse fields. The material observed in the present study combined two different types of stainless steels, i.e. 15–5 PH martensitic stainless steel and SAF 2507 duplex steel. The synergy effect between these alloys is very valuable for developing functional gradient materials with unique and optimized properties for various applications. As the individual alloys produced by conventional and advanced AM methods have been subjected to detailed studies [6, 8, 9, 11, 12, 18, 20, 28–30], especially separately, present study is first and foremost focused on the interface between these materials.

In the present study, the exceptional metallurgical bonding observed at the interface of the functionally graded materials showed no visible defects, including pores, hot cracks, liquation and solidification cracks, or any other structural flaws. Zhang [31] reported the absence of any defects in the graded material U75V/15-5PH, as well as in a FGM

composed of stainless steel 316L and hot work tool steel H13, as studied by Hengsbach [32]. Liang et al. in [33] observed also similar phenomenon in the interfacial characteristics of joined austenitic 316L and 15–5 PH with presence of few pores. This stands in contrast to studies between Fe and Ni alloys, for example in the 316L / Inconel 718 investigated by Melzer [2, 3], Yang [34] and Koukolíková [23], type Inconel 718 / Inconel 738 investigated by Zhang [35], where above mentioned defects were observed near the interface.

Since the change in chemical composition (Table 4), especially the increased nickel content, caused a change in the solidification mode, it was important to identify the individual phases formed at the interface of the FGM. Metallographic analysis by means of light and electron microscopy supported by EDS and EBSD analyses identified the presence of austenitic (FCC) and ferritic (BCC) crystal structure phases at the interface regions of the FGM material. Nevertheless, SAF 2507 and 15–5 PH are two specific materials that possess low carbon content with a BCC structure of ferritic and martensitic phase [14]. Distinguishing martensite from ferrite based on EBSD analysis can be challenging, as investigated by Nowell et al. [36], who explored several EBSD image analysis-based approaches for this purpose. However, the identification of crystallographically similar phases like ferrite and martensite can be improved through the application of etching procedures, as demonstrated by Mandal [37] using a colour etching technique. Therefore, it was crucial to employ the aforementioned method to differentiate between these phases at the interface of the FGM. To achieve this, the colour etching technique was utilized, specifically using Beraha II etchant with a $K_2S_2O_5$ agent. This approach was chosen as the Villela–Bain etchant proved ineffective in the interface region. Exposing the SAF 2507 microstructure in Fig. 8 a, b resulted in the coloration of ferrite (brown or blue) while the austenite remained light [11, 12, 19], and

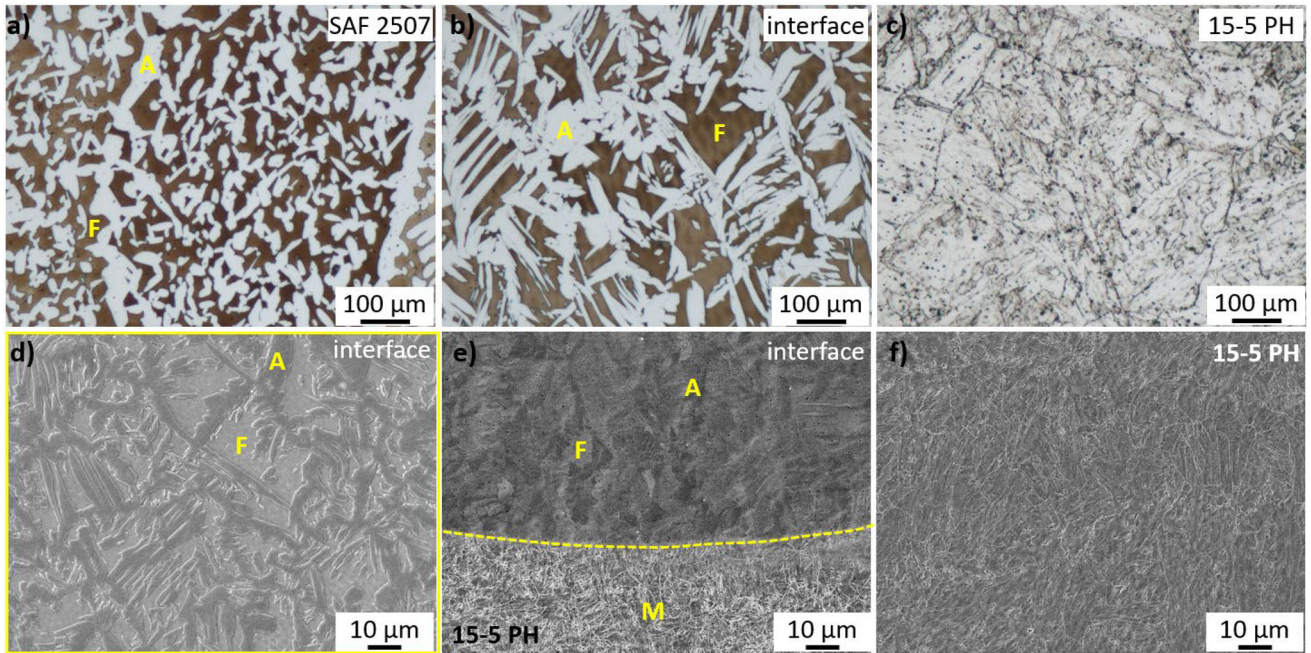


Figure 8 Microstructural morphological features distinguished by LM and SEM: **a** microstructure of SAF 2507 (LM); **b** microstructure of the interface (LM); **c** martensitic microstructure of 15–5 PH (LM); **d** detailed microstructure of the interface (SEM); **e** overview microstructure (SEM); **f** martensitic microstructure of 15–5 PH (SEM).

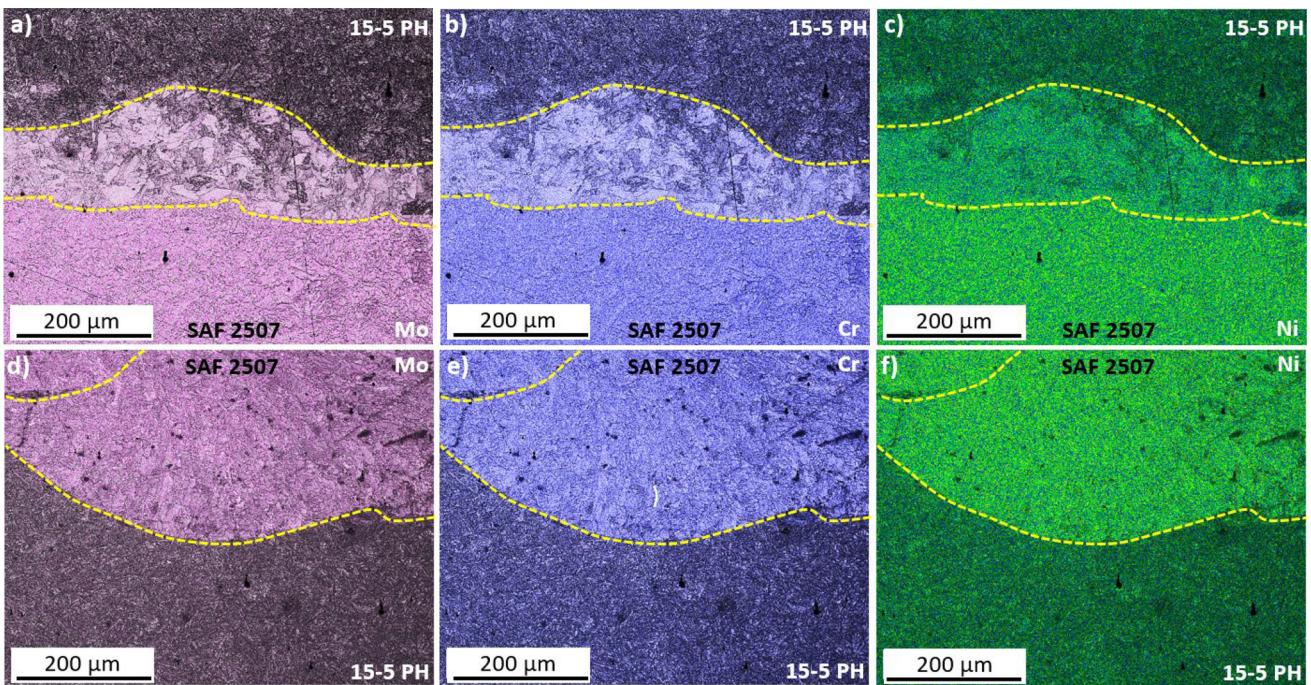


Figure 9 EDS maps: **a** Mo distribution along the interface I_SA_480; **b** Cr distribution along the interface I_SA_480; **c** Ni distribution along the interface I_SA_480; **d** Mo distribution along the interface II_SA_480; **e** Cr distribution along the interface II_SA_480; **f** Ni distribution along the interface II_SA_480.

martensite appeared almost black (Fig. 2). Another distinguishing factor was the morphology of the

distinct phases, with ferrite exhibiting a smooth surface (Fig. 8 a, b, d), whereas martensite displayed

distinctive morphological features (Fig. 8 c, f). These morphological differences were effectively observed and differentiated using both light and scanning electron microscopy (Fig. 8 b, e).

The comprehensive analysis of the EDS results provided compelling evidence for the role of Mo, Cr, and Ni in facilitating element diffusion within MTZ. Figure 9 demonstrates specific examples that establish a correlation between the diffusion of these elements and the resulting chemical composition. The EDS maps clearly depict the alignment of element content with the original alloy composition (Table 4), confirming their involvement in the diffusion processes. Additionally, the gradual transition of these elements at the interface, as indicated by changing colour intensity in the EDS maps, offers valuable insights into the gradual variations in elemental composition within the analysed samples. In contrast to the findings of Liang et al. [33], which showed no distinct morphological features or significant compositional changes at the interface of 316L / 15–5 PH, present study demonstrated clear evidence of Mo (Fig. 9 a, d), Cr (Fig. 9 b, e), and Ni (Fig. 9 c, f) diffusion. These diffusion processes were found to play a significant role in the observed microstructural

changes, providing validation for their influence on the investigated materials.

The microstructural change at the interface captured in Fig. 10 is influenced by factors such as cooling rate, alloy composition, and processing conditions. Alloying element such as nickel helps to promote the austenite phase. The effect of Ni on the resulting microstructure of a heterogeneous weld, although for conventional TIG welding of ferritic (FSS-AISI 430) and austenitic steel (ASS-AISI 304), has been described in detail by Zhang [38]. The authors of [38] observed that the mixing of two dissimilar materials in a joint led to the formation of a duplex phase feature in the FZ, as the introduction of additional Ni into the welding pool caused a significant alteration in the solidification mode. The impact of adding Ni to a melt pool extends beyond this specific case, as it has been found to have a substantial influence on the solidification behaviour of the alloys. In the case of 15–5 PH alloy, increasing the nickel content primarily served to stabilize the austenite phase at lower transformation temperatures, effectively impeding the formation of martensite by lowering the martensite start temperature (M_s). This finding is consistent with the research of Keehan [39] and Vunnam [40], who observed a

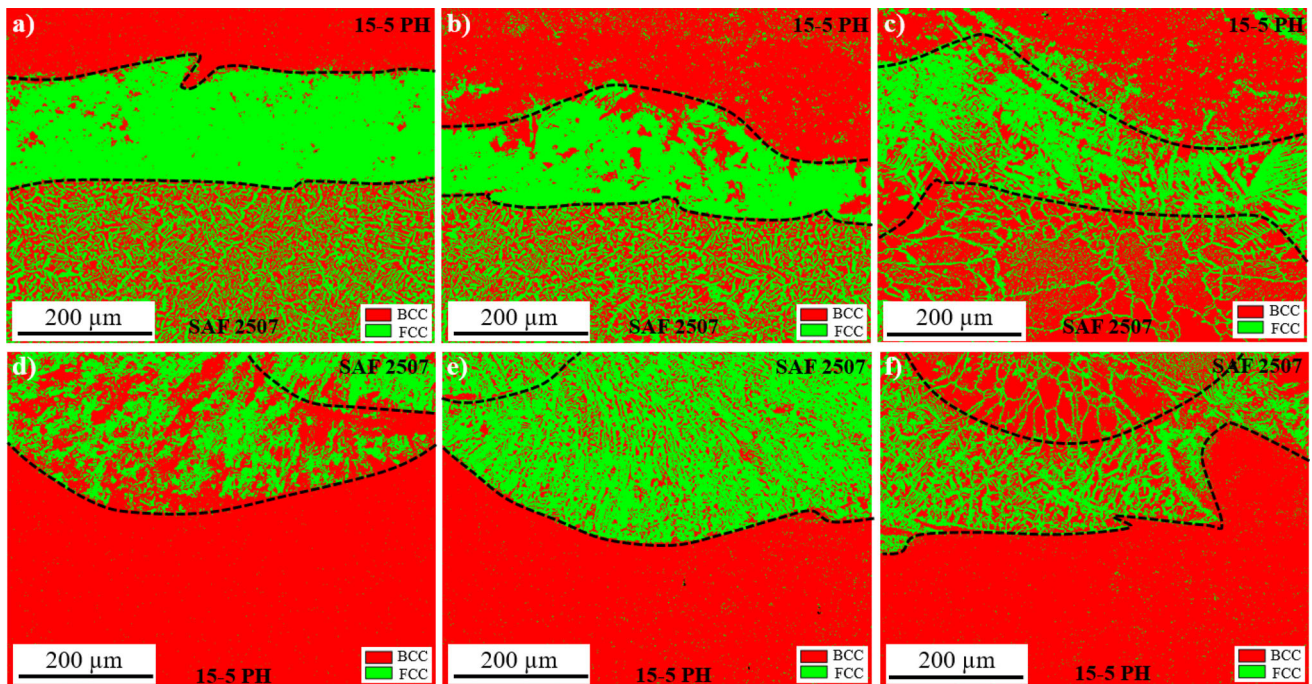


Figure 10 EBSD phase maps: **a** interface I_SA; **b** interface I_SA_480; **c** interface I_480; **d** interface II_SA; **e** interface II_SA_480; **f** interface II_480.

Table 8 Phase fraction determined by EBSD analysis. Cropped in OIM Analysis™

Sample	Phase fraction		Sample	Phase fraction	
	α / α'	γ		α / α'	γ
I_SA	8	92	II_SA	52	48
I_SA_480	36	63	II_SA_480	30	70
I_SA_620	24	76	II_SA_620	28	72
I_480	48	52	II_480	46	54
I_620	31	69	II_620	54	46

decrease in the martensitic transformation temperature (M_s) with increasing nickel content in steel.

Table 8 displays the phase composition of the extracted interfaces analysed using EBSD in OIM software, indicating that the SA-treated states (Fig. 10 a, b, d, e) are predominantly composed of the austenitic phase.

Lippold and Koukal [41, 42] proposed a mechanism for the crystallization process at the interface in the fusion zone. According to their proposal, the crystallization process is initiated through the epitaxial nucleation due to remelting of previously solidified material with the solidification sequence as outlined in Vunnam's research [40], meaning that the newly formed grains maintain the same crystallographic orientation and size as the original stainless steel grains. As a result, the grain boundaries remained continuous across the fusion zone boundary, suggesting that there was no significant change in the microstructure and the grain boundaries were continuous across the fusion zone boundary (Figs. 3, 4).

An interesting aspect to the influence of the sequence of the materials on the size and shape of the newly deposited material was observed. The fusion zones have a different appearance between the interface I and interface II. EBSD maps (Figs. 11a, d, g and 12a, d, g) proved the shape of interface I appears almost linear (flat), while interface II follows the shape of the melt pools. The preservation of continuous grain boundaries across the fusion zone is observed in newly formed grains, which maintained both the same crystallographic orientation and size as the original grains. This phenomenon has also been observed in previous studies of Lippold [41] and Koukolikova et al. [23].

Potential grain recrystallization at the interface was explored by the grain misorientation spread (GOS) maps (Figs. 11b, e, h and 12b, e, h). Blue colour indicates the presence of grains with GOS values $< 1^\circ$, which is a criterion to separate potentially recrystallized grains [12, 33]. The dominance of potentially recrystallized grains at the interface II over the interface I may be attributed to various factors, suggesting that the two interfaces may have undergone different degrees of recrystallization. Liang et al. in [33] observed this phenomenon in the interfacial characteristics of austenitic 316L and martensitic 15–5 PH, reported that recrystallization has been documented in various studies, even in the absence of post-processing heat treatments, and was often attributed to the thermal cycles induced by the layer-by-layer scanning process. Soysal et al. [43] suggested that this phenomenon was caused by the difference in alloy's melting points and the flow characteristics of the melt pool. Due to the different temperature intervals of the solidus and liquidus of the martensitic steel and duplex steel (15–5 PH: 1404–1440 °C and SAF 2507: 1350 °C), the subsequent application of 15–5 PH steel to SAF 2507 resulted in its partial melting, which matched well the findings of Melzer [2], Chen [5] and [23]. The authors of [23] related also to the difference in coefficient of thermal expansion of individual materials.

A formation of a fine-grained equiaxed FGM microstructure at the interface I was observed after SA heat treatment, whereas the grains of the SAF 2507 deposited onto martensitic steel (interface II) exhibited a columnar grain growth pattern that followed the direction of maximum thermal gradient. Nevertheless the orientation of the austenite and ferrite grains in the interfaces is relatively random with a low texture intensities (Figs. 11 c, f, i and 12 c, f, i).

Figure 13 presents the misorientation-angle distributions of the austenite–ferrite interfaces within the interface microstructures of samples with SA + PH at 480 °C and direct PH at 480 °C (samples I_SA_480, I_480 and II_SA_480, II_480). The colour coded grain boundaries combined with the EBSD Image Quality (IQ) maps correspond to specific misorientation angles, effectively representing the distribution of these angles across the interfaces. In the context of grain boundaries, it is worth noting that high-angle boundaries are defined as those with a misorientation angle exceeding 15° [23]. The 15–5 PH material

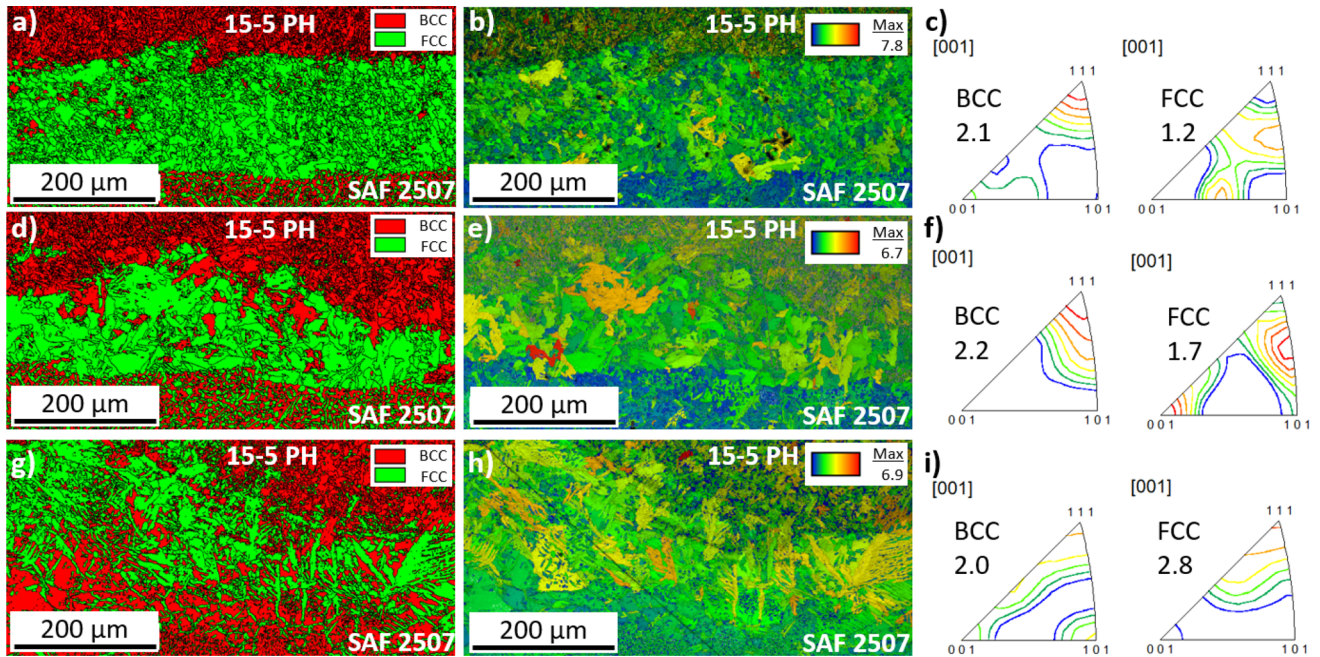


Figure 11 Interface I: **a** EBSD phase map sample I_SA; **b** GOS map sample I_SA; **c** IPF sample I_SA; **d** EBSD phase map sample I_SA_480; **e** GOS map sample I_SA_480; **f** IPF sample

I_SA_480; **g** EBSD phase map sample I_480; **h** GOS map sample I_480; **i** IPF sample I_480.

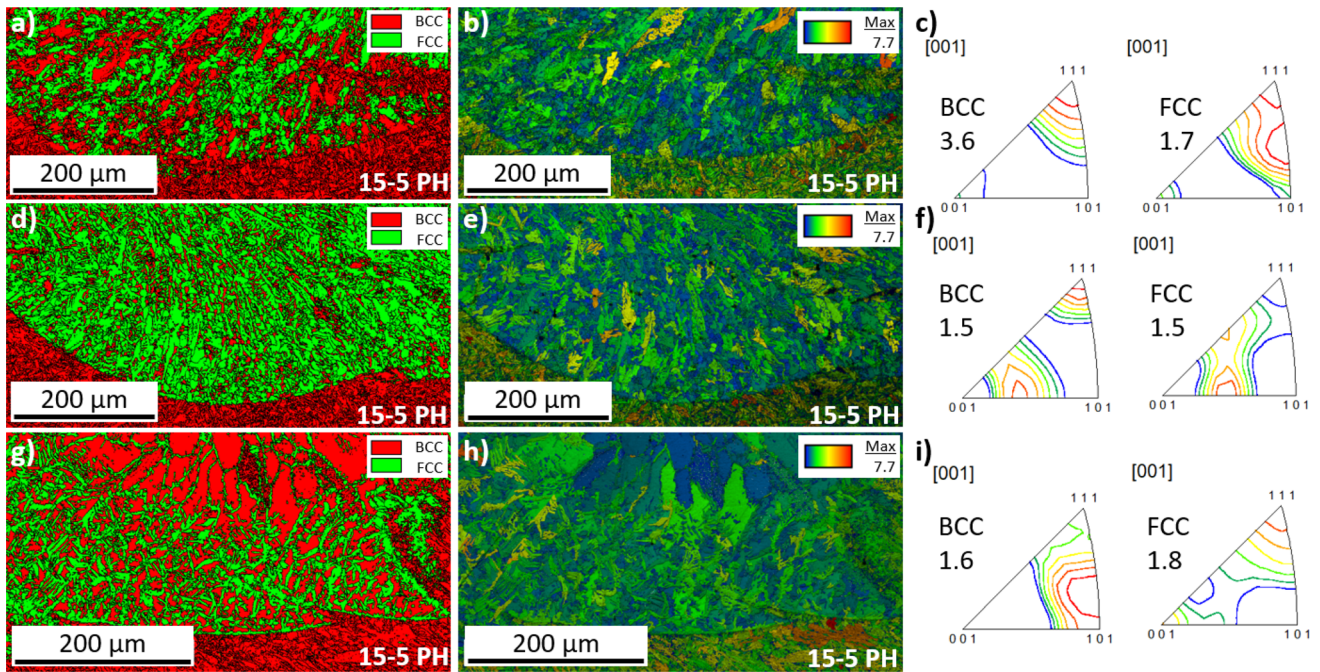


Figure 12 Interface II: **a** EBSD phase map sample II_SA; **b** GOS map sample II_SA; **c** IPF sample II_SA; **d** EBSD phase map sample II_SA_480; **e** GOS map sample II_SA_480; **f** IPF sample

II_SA_480; **g** EBSD phase map sample II_480; **h** GOS map sample II_480; **i** IPF sample II_480.

demonstrated elevated levels of misorientation angles, surpassing high-angle boundaries with misorientation angles 50° in particular, whereas the

SAF 2507 regions fall within the range of $40\text{--}50^\circ$. With regard to interface I and interface II, they exhibit distinct boundaries spanning the entire interval of

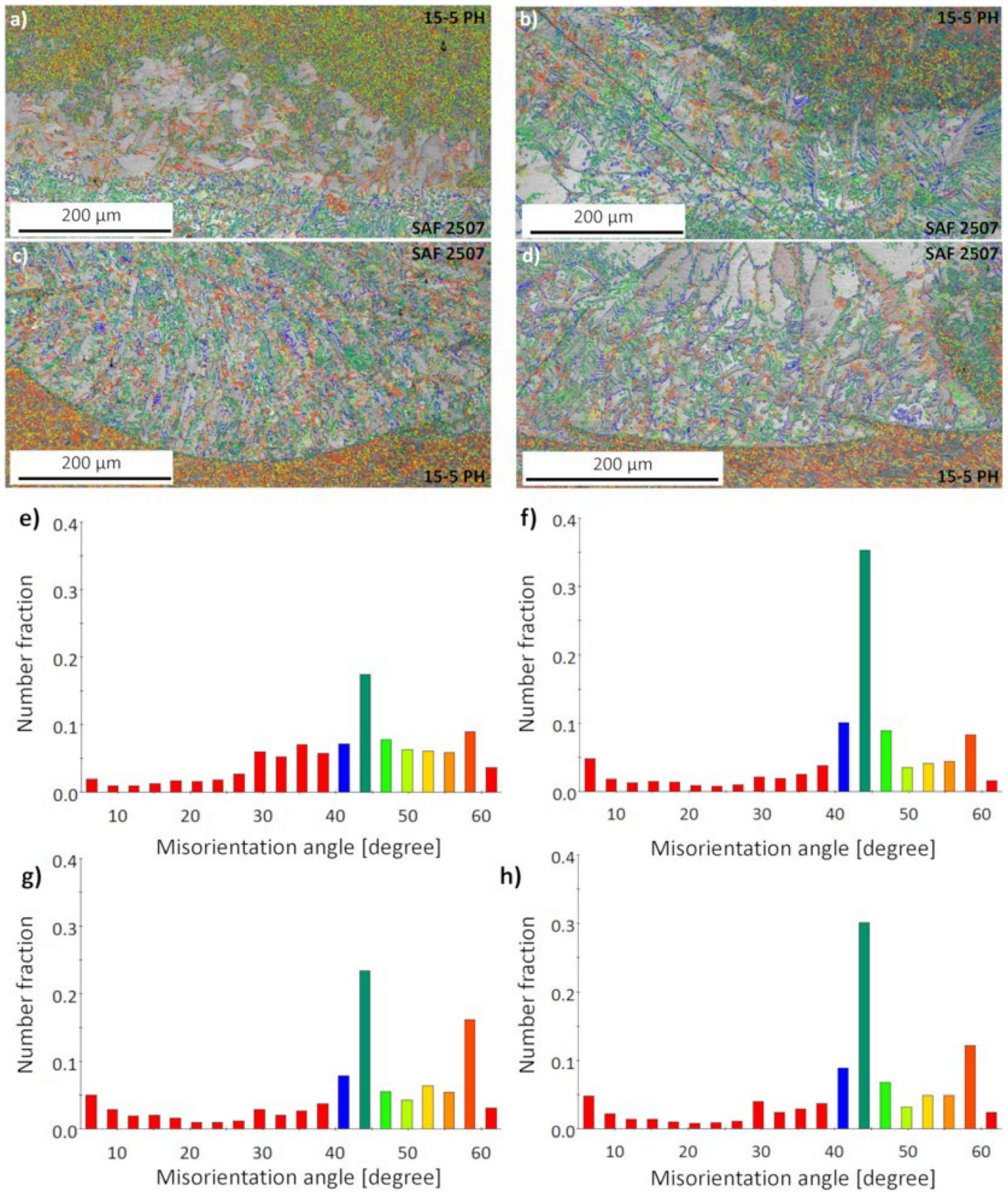


Figure 13 Misorientation post-processing in OIM Analysis™ software: **a** IQ map with GB-interface I_SA_480; **b** IQ map with GB-interface I_480; **c** IQ map with GB-interface II_SA_480; **d** IQ map with GB-interface II_480; **e** misorientation-angle

distribution-interface I_SA_480; **f** misorientation-angle distribution-interface I_480; **g** misorientation-angle distribution-interface II_SA_480; **h** misorientation-angle distribution-interface II_480.

40–65°. The prevalence of high-angle boundaries throughout the entire FGM is evident from the analysis conducted. All distributions in Fig. 13e–h exhibit a prominent peak at 44°. This misorientation angle aligns with the orientation relationship models extensively investigated by Haghdadi et al. [44, 45], which are associated to the BCC to FCC transformation. However, it is noteworthy that the peak intensity for samples subjected to direct ageing (I_480 and II_480) is roughly twice as high as that observed for microstructures I_SA_480 and II_SA_480.

It should be noted that recorded data of elastic modulus measurement (Fig. 5a) were distinguished by relatively high scatter, observable especially for the interface I (batches SA, SA_620 and 620). The elastic modulus measurement using miniaturized specimens should be interpreted cautiously. According to the study [46], the data measured during uniaxial tensile test using miniaturized specimens does not provide the Young's modulus values with high precision. The uniaxial testing can be affected by several factors, which include clamp effect or specimen alignment, described in more detail in standard ASTM E-111 [47]. Therefore, Zhang et al. [46] recommend application of nondestructive methods such as ultrasound and thermomechanical techniques. However, these are out of the scope of this study. On the other hand, the authors stated that miniaturized tensile test can provide repeatable tensile characteristics in terms of strength and elongation, which are comparable with the results, obtained using standard testing specimens.

Results presented in Table 6 and Fig. 5b, c, provided valuable insights into the effects of heat treatment on the strength of materials at different interfaces. The fracture was predominantly observed in the part of the specimen made of SAF 2507, which is characterized by lower strength. The PH level exerted a significant influence on the properties of 15–5 PH and played a central role in determining the behaviour of the entire FGM. The FGM part on the 15–5 PH side exhibited peak hardness at 480 °C, resulting in a notable increase in its strength. As a result, the predominant deformation occurred within the duplex steel region of the FGM. However, the hardness measurements presented in Table 5 indicated that the lowest hardness values were observed at the interfaces. This observation seems inconsistent with the fact that the fracture prevailed in the SAF2507 material instead at softer interfaces

(Table 7). To explain this inconsistency, several factors need were considered. Firstly, hardness measurements provided an indication of a material's resistance to localized deformation, but they did not necessarily correlated directly with material's yield strength. Secondly, yield strength represents the point at which the material transitions from elastic to plastic behaviour. SAF 2507 exhibits higher elongation and easier deformation compared to 15–5 PH steel due to its lower yield strength, which was confirmed from several studies summarized in Table 9. This observation was also confirmed during the MTT measurements using digital image correlation to track and analyse deformation during testing. Through a series of experiments, it was demonstrated that SAF 2507 underwent greater deformation as is demonstrated in Fig. 14. The interface is highlighted by yellow dashed line. Different stages of deformation are captured in an undeformed sample (Fig. 14a), a sample showing the presence of necking (Fig. 14b) with final fracture, and a fracture in the SAF 2507 region (Fig. 14c) observed by LM in DIC mode. After reaching the yield strength and subsequent plastic deformation, a neck formation occurred in SAF 2507, resulting in stress localization in this region. Therefore, the hardness did not reflect the differences in yield strength between the materials' regions.

Zhang et al. [38] reported transition of local mechanical properties in the ASS/FSS joints, which was also monitored by the digital image correlation to detect the deformation during the testing.

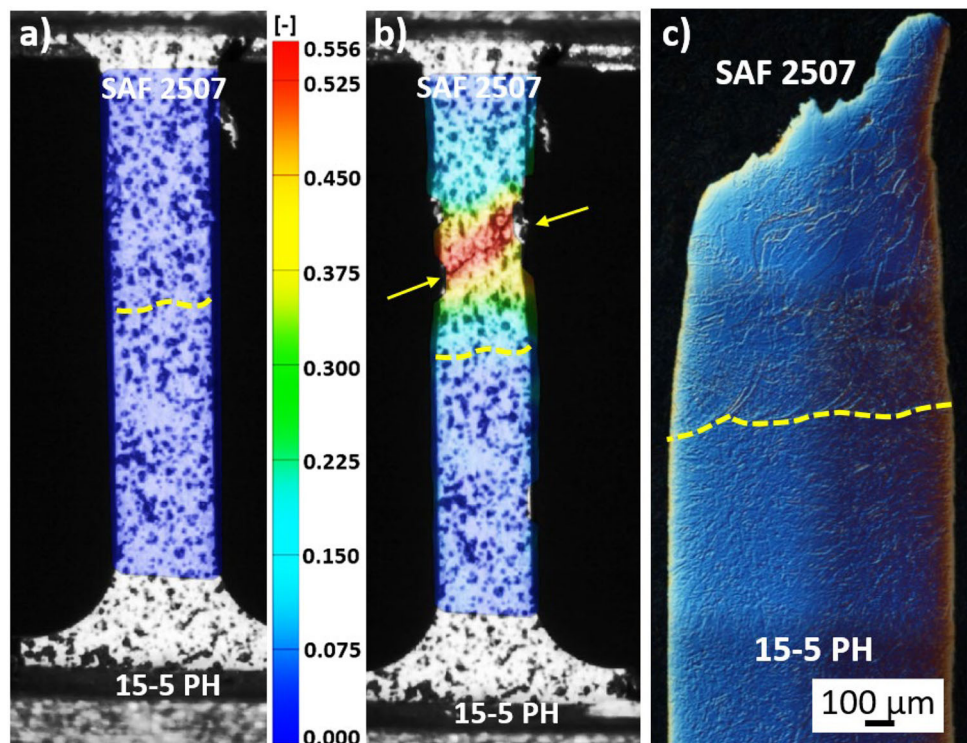
The results of the authors [38] followed the same trend of strain growth rate as in the present study, i.e. the material that exhibited lower tensile strength experienced faster strain growth rate until necking and fracture occurred subsequently.

Several studies [8, 9, 11, 12, 14, 29, 31, 32, 48, 49] have focused on investigating the mechanical properties of individual AM materials in both the as-built and heat-treated states. Table 9 provides a summary of the comparison of the mechanical properties of two materials, SAF 2507 and 15–5 PH, in both their as-deposited and heat-treated states. Table also establishes the results for the functionally graded material (FGM) that was created by combining the two materials. Salvetr et al. [12] demonstrated that balanced austenite–ferrite ratio (50:50) was achieved for DED duplex steel SAF 2507 through the solution annealing at 1100 °C / 1 h followed by WQ. Such

Table 9 Summary for the SAF2507 and 15-5PH mechanical properties in heat-treated conditions

Material	Ref	Method	Heat treatment	UTS [MPa]	YS [MPa]	El [%]
15-5PH	[8]	DED	AB	1121		4
15-5PH	[45]	L-PBF	AB	940	850	10
15-5PH	[9]	DED	AB	1097		7
			aged 450 °C	1397		2
15-5PH	[14]	Forged	SA 1040 °C/7 h, AC, aged 450 °C / 4 h, AC	1362	964	17
			SA 1040 °C/7 h, AC, aged 625 °C / 4 h, AC	963	739	20
SAF 2507	[46]	L-PBF	AB	950	820	15
		Wrought		860	610	20
SAF 2507	[12]	DED	AB	832	682	17
SAF 2507			SA	754	549	30
SAF 2507	[11]	DED	AB	830	680	15
SAF 2507			SA	760	540	30
U75V/15-5 PH	[31]	DED	AB	530	882	10
316L / H13	[32]	L-PBF	AB	570		20
SAF 2507/15-5 PH	*	DED	SA 1040 °C/1 h, WQ, aged 480 °C / 1 h, WQ	I 873 II 840	623 603	13 15
SAF 2507/15-5 PH	*	DED	SA 1040 °C/1 h, WQ, aged 620 °C / 1 h, WQ	I 811 II 804	569 575	20 20

Figure 14 Different stages of deformation in sample II_620 with equivalent von Mises strain [-]: **a** an undeformed sample; **b** a sample showing the presence of necking and crack in SAF 2507 region; **c** after fracture metallographic section (LM/DIC) of a MTT sample with a presence of crack in the SAF 2507 region.



heat treatment provided UTS strength of 754 MPa and an elongation of 30%. The values for 316L/H13 [32] and U75V/15-5PH [31] were shown as reference in order to provide comparative data for FGM

materials. The present study provided valuable information about the material’s performance under SA and ageing at 480 °C and 620 °C specific conditions. The abbreviation AC in table stands for air

cooling, * present study. According to Haghdadadi [13] and Jiang [49], the reason for the individual alloy mechanical properties' improvement can be attributed to the high density of dislocations in the AM microstructures.

However, it is important to consider other factors such as corrosion resistance, as SAF 2507 achieves optimum corrosion resistance with microstructural balance, which is declared after SA [15]. Therefore, the SA_480 heat treatment may be the most suitable heat treatment for achieving the desired mechanical properties in practical applications of the FGMs from stainless steels. The specific mechanical properties that are of the interest may vary depending on the application, but it appears that the SA_480 heat treatment is a good starting point for achieving sufficient hardness and strength values of the functionally graded materials.

Conclusions

Functionally graded materials 15–5 PH / SAF 2507 subjected to post-processing heat treatment are good potential candidates for harsh corrosion environments. In terms of microstructure, interface quality, and mechanical properties, the applied DMT mode was found to be optimal for these types of functionally graded materials with crack-free interfaces. The research observed the influence of the heat treatment and the consequences of application alternatives of SAF 2507 and 15–5 PH on the quality of the functionally graded materials' interfaces. The main aspects of this research have been drawn:

- The heterogeneous 15–5 PH / SAF 2507 interface solidified with an important change in the interface composition. This caused the interface between the microstructural transition zone and 15–5 PH / SAF 2507 to undergo a dramatic modification in the microstructure.
- Following the solution annealing and solution annealing with precipitation hardening, the formation of a fine-grained almost equiaxed microstructure was observed at interface I, whereas the grains of the SAF 2507 deposited onto martensitic steel (interface II) exhibited a columnar grain growth pattern that followed the direction of maximum thermal gradient. Nevertheless, the orientation of the austenite and ferrite grains in the interfaces is relatively random with low texture intensities.
- The comprehensive analysis of the EDS results provided strong evidence supporting the significant role of Mo, Cr, and Ni in facilitating element diffusion processes within the microstructural transition zone, as demonstrated by the correlation between diffusion and resulting chemical composition, confirming their contribution to observed microstructural changes.
- The sequence of the materials' application did not have a significant effect on their final mechanical tensile properties in the heat-treated states. The SAF 2507 and 15–5 PH stainless steels are commonly used in the solution annealed and hardened conditions, these resulting mechanical properties were of the highest interest. The interface I reached YS 623 MPa, UTS 873 MPa with 13% elongation and the interface II reached YS 603 MPa, UTS 840 MPa with 15% elongation.
- The PH level had a pronounced impact on the characteristics of the 15–5 PH material and assumed a dominant role in the overall behaviour of the FGM. The attainment of maximum hardness at 480 °C for the 15–5 PH alloy resulted in a substantial enhancement in the strength of the FGM component on the 15–5 PH side, consequently leading to predominant deformation within the region of the duplex steel.
- The final fractures occurred in mainly in the SAF 2507 regions. A larger fraction of austenite at the interface led to drop in the hardness at the interface. However, the changes in the hardness values at the interface correlated with the changes in the microstructure (interface I reached 249 HV5, interface II reached 251 HV5).
- The inconsistency between hardness measurements and the fracture behaviour in this study was explained by considering factors such as the lower yield strength, higher elongation, and easier deformation of SAF 2507 compared to 15–5 PH steel, which were confirmed by MTT measurements and deformation analysis.
- The research highlights the design flexibility of FGM SAF 2507/15–5 PH stainless steel.

Acknowledgements

The paper was supported from ERDF Research of advanced steels with unique properties, CZ.02.1.01/0.0/0.0/16_019/0000836. This research was also funded by SLOVENIAN RESEARCH AGENCY, grant number P2-0132 and L2-4445.

Author contributions

MK contributed to conceptualization, investigation, and writing—original draft. **PP** contributed to supervision, writing—review and editing. **SR** contributed to investigation, writing—review and editing. **MB** contributed to investigation. **AK** contributed to validation, writing—review and editing.

Declarations

Conflict of interest The authors declare that they have no known competing financial interests or personal relationships that could have appeared to influence the work reported in this paper.

References

- [1] Saleh B, Jiang J, Fathi R et al (2020) 30 Years of functionally graded materials: an overview of manufacturing methods, applications and future challenges. *Compos Part B Eng* 201:108376. <https://doi.org/10.1016/j.compositesb.2020.108376>
- [2] Melzer D, Džugan J, Koukolíková M et al (2021) Structural integrity and mechanical properties of the functionally graded material based on 316L/IN718 processed by DED technology. *Mater Sci Eng A*. <https://doi.org/10.1016/j.msea.2021.141038>
- [3] Melzer D, Džugan J, Koukolíková M et al (2022) Fracture characterisation of vertically build functionally graded 316L stainless steel with inconel 718 deposited by directed energy deposition process. *Virtual Phys Prototyp* 17:821–840. <https://doi.org/10.1080/17452759.2022.2073793>
- [4] Xiao Y, Wan Z, Liu P et al (2022) Quantitative simulations of grain nucleation and growth at additively manufactured bimetallic interfaces of SS316L and IN625. *J Mater Process Technol* 302:117506. <https://doi.org/10.1016/j.jmatprotec.2022.117506>
- [5] Chen N, Khan HA, Wan Z et al (2020) Microstructural characteristics and crack formation in additively manufactured bimetal material of 316L stainless steel and Inconel 625. *Addit Manuf* 32:101037. <https://doi.org/10.1016/j.addma.2020.101037>
- [6] Mészáros I, Bögre B (2019) Complex study of eutectoidal phase transformation of 2507-type super-duplex stainless steel. *Materials (Basel)*. <https://doi.org/10.3390/ma12132205>
- [7] Sam M, Jojith R, Radhika N (2021) Progression in manufacturing of functionally graded materials and impact of thermal treatment—A critical review. *J Manuf Process* 68:1339–1377. <https://doi.org/10.1016/j.jmapro.2021.06.062>
- [8] Chen W, Xu L, Zhang Y et al (2022) Additive manufacturing of high-performance 15–5PH stainless steel matrix composites. *Virtual Phys Prototyp* 17:366–381. <https://doi.org/10.1080/17452759.2021.2019793>
- [9] Chen W, Xu L, Hao K et al (2023) Effect of heat treatment on microstructure and performances of additively manufactured 15–5PH stainless steel. *Opt Laser Technol* 157:108711. <https://doi.org/10.1016/j.optlastec.2022.108711>
- [10] Kultz Unti LF, Aota LS, Jardini AL et al (2021) Microstructural characterization of 15–5PH stainless steel processed by laser powder-bed fusion. *Mater Charact*. <https://doi.org/10.1016/j.matchar.2021.111485>
- [11] Brázda M, Salvetr P, Rzepa S et al (2021) Effect of heat treatment on mechanical properties of duplex steel SAF 2507 manufactured by DED. *IOP Conf Ser Mater Sci Eng* 1178:012008. <https://doi.org/10.1088/1757-899x/1178/1/012008>
- [12] Salvetr P, Školáková A, Melzer D et al (2022) Characterization of super duplex stainless steel SAF2507 deposited by directed energy deposition. *Mater Sci Eng A*. <https://doi.org/10.1016/j.msea.2022.144084>
- [13] Haghdaei N, Laleh M, Moyle M, Primig S (2021) Additive manufacturing of steels: a review of achievements and challenges. *J Mater Sci* 56:64–107. <https://doi.org/10.1007/s10853-020-05109-0>
- [14] Kumar VA, Karthikeyan MK, Gupta RK et al (2012) Aging behavior in 15–5 ph precipitation hardening martensitic stainless steel. *Mater Sci Forum* 710:483–488. <https://doi.org/10.4028/www.scientific.net/MSF.710.483>
- [15] Bieczma MV, Martin U, Linhardt P et al (2021) Non-destructive techniques for the detection of sigma phase in duplex stainless steel: a comprehensive review. *Eng Fail Anal*. <https://doi.org/10.1016/j.engfailanal.2021.105227>
- [16] Taban E, Kaluc E (2011) Welding behaviour of duplex and superduplex stainless steels using laser and plasma arc welding processes. *Weld World* 55:48–57. <https://doi.org/10.1007/BF03321307>
- [17] (2023) Osprey ® 2507 Super-duplex stainless steel for additive manufacturing datasheet. <https://www.additive.sandvik/en/super-duplex/super-duplex-powder-for-additive-manu>

- facturing/material-data-osprey-2507-super-duplex-stainless-steel/
- [18] Peng XY, Zhou XL, Hua XZ et al (2015) Effect of aging on hardening behavior of 15–5 PH stainless steel. *J Iron Steel Res Int* 22:607–614. [https://doi.org/10.1016/S1006-706X\(15\)30047-9](https://doi.org/10.1016/S1006-706X(15)30047-9)
- [19] Muthupandi V, Bala Srinivasan P, Seshadri SK, Sundaresan S (2003) Effect of weld metal chemistry and heat input on the structure and properties of duplex stainless steel welds. *Mater Sci Eng A* 358:9–16. [https://doi.org/10.1016/S0921-5093\(03\)00077-7](https://doi.org/10.1016/S0921-5093(03)00077-7)
- [20] Köse C, Topal C (2022) Texture, microstructure and mechanical properties of laser beam welded AISI 2507 super duplex stainless steel. *Mater Chem Phys*. <https://doi.org/10.1016/j.matchemphys.2022.126490>
- [21] Zhang Z, Zhao H, Zhang H et al (2017) Microstructure evolution and pitting corrosion behavior of UNS S32750 super duplex stainless steel welds after short-time heat treatment. *Corros Sci* 121:22–31. <https://doi.org/10.1016/j.corsci.2017.02.006>
- [22] Wei C, Li L, Zhang X, Chueh YH (2018) 3D printing of multiple metallic materials via modified selective laser melting. *CIRP Ann* 67:245–248. <https://doi.org/10.1016/j.cirp.2018.04.096>
- [23] Koukolíková M, Simson T, Rzepa S et al (2022) The influence of laser power on the interfaces of functionally graded materials fabricated by powder-based directed energy deposition. *J Mater Sci* 57:13695–13723. <https://doi.org/10.1007/s10853-022-07453-9>
- [24] Godec M, Malej S, Feizpour D et al (2021) Hybrid additive manufacturing of Inconel 718 for future space applications. *Mater Charact*. <https://doi.org/10.1016/j.matchar.2020.110842>
- [25] Rzepa S, Trojanová Z, Džugan J et al (2023) Effect of ECAP processing on microstructure and mechanical behaviour of Ti-6Al-4V manufactured by directed energy deposition. *Mater Charact* 196:112622. <https://doi.org/10.1016/j.matchar.2022.112622>
- [26] Andreiev A, Hoyer KP, Dula D et al (2021) Laser beam melting of functionally graded materials with application-adapted tailoring of magnetic and mechanical performance. *Mater Sci Eng A* 822:141662. <https://doi.org/10.1016/j.msea.2021.141662>
- [27] Hu Z, Ma Z, Yu L, Liu Y (2023) Functionally graded materials with grain-size gradients and heterogeneous microstructures achieved by additive manufacturing. *Scr Mater* 226:115197. <https://doi.org/10.1016/j.scriptamat.2022.115197>
- [28] Chen W, Luan JH, Xu L et al (2022) Reversed austenite in additively manufactured martensitic stainless steel. *Mater Sci Eng A* 834:142597. <https://doi.org/10.1016/j.msea.2022.142597>
- [29] Kumar P, Sharma SK, Singh RKR (2022) Recent trends and future outlooks in manufacturing methods and applications of FGM: a comprehensive review. *Mater Manuf Process*. <https://doi.org/10.1080/10426914.2022.2075892>
- [30] Zhang J, Yu M, Li Z et al (2021) The effect of laser energy density on the microstructure, residual stress and phase composition of H13 steel treated by laser surface melting. *J Alloys Compd* 856:158168. <https://doi.org/10.1016/j.jallcom.2020.158168>
- [31] Zhang B, Wang H, He B et al (2022) Microstructure and mechanical properties of directed energy deposited U75V/15–5PH structurally graded material. *J Alloys Compd* 898:163001. <https://doi.org/10.1016/j.jallcom.2021.163001>
- [32] Hengsbach F, Koppa P, Holzweissig MJ et al (2018) Inline additively manufactured functionally graded multi-materials: microstructural and mechanical characterization of 316L parts with H13 layers. *Prog Addit Manuf* 3:221–231. <https://doi.org/10.1007/s40964-018-0044-4>
- [33] Liang A, Sahu S, Zhao X et al (2023) Materials characterization interfacial characteristics of austenitic 316 L and martensitic 15–5PH stainless steels joined by laser powder bed fusion. *Mater Charact* 198:112719. <https://doi.org/10.1016/j.matchar.2023.112719>
- [34] Yang SW, Yoon J, Lee H, Shim DS (2022) Defect of functionally graded material of inconel 718 and STS 316L fabricated by directed energy deposition and its effect on mechanical properties. *J Mater Res Technol* 17:478–497. <https://doi.org/10.1016/j.jmrt.2022.01.029>
- [35] Zhang X, Chai Z, Chen H et al (2021) A novel method to prevent cracking in directed energy deposition of inconel 738 by in-situ doping inconel 718. *Mater Des* 197:109214. <https://doi.org/10.1016/j.matdes.2020.109214>
- [36] Nowell MM, Wright SI, Carpenter JO (2009) Differentiating ferrite and martensite in steel microstructures using electron backscatter diffraction. *Mater Sci Technol Conf Exhib 2009, MS T'09* 2:933–943
- [37] Mandal M, Aashranth B, Samantaray D, Vasudevan M (2022) Improvements in the metallography of ferritic–martensitic steels through a color etching procedure. *Metallogr Microstruct Anal* 12:49–61. <https://doi.org/10.1007/s13632-022-00916-0>
- [38] Zhang X, Zhang Y, Wu Y et al (2019) Effects of melting-mixing ratio on the interfacial microstructure and tensile properties of austenitic – ferritic stainless steel joints. *Integr Med Res* 8:2649–2661. <https://doi.org/10.1016/j.jmrt.2018.12.025>
- [39] Keehan E, Karlsson L, Andren HO (2006) Influence of carbon, manganese and nickel on microstructure and

- properties of strong steel weld metals: part 1 - Effect of nickel content. *Sci Technol Weld Join* 11:1–8. <https://doi.org/10.1179/174329306X77830>
- [40] Vunnam S, Saboo A, Sudbrack C, Starr TL (2019) Effect of powder chemical composition on the as-built microstructure of 17–4 PH stainless steel processed by selective laser melting. *Addit Manuf* 30:100876. <https://doi.org/10.1016/j.addma.2019.100876>
- [41] JC Lippold 2014 *Welding Metallurgy and Weldability* Wiley
- [42] Koukal J et al (2020). *Materials and their behaviour during welding*. Ostrava
- [43] Soysal T, Kou S, Tat D, Pasang T (2016) *Acta Materialia* Macrosegregation in dissimilar-metal fusion welding. *Acta Mater* 110:149–160. <https://doi.org/10.1016/j.actamat.2016.03.004>
- [44] Haghdad N, Cizek P, Hodgson PD et al (2018) Effect of ferrite-to-austenite phase transformation path on the interface crystallographic character distributions in a duplex stainless steel. *Acta Mater* 145:196–209. <https://doi.org/10.1016/j.actamat.2017.11.057>
- [45] Haghdad N, Ledermueller C, Chen H et al (2022) Evolution of microstructure and mechanical properties in 2205 duplex stainless steels during additive manufacturing and heat treatment. *Mater Sci Eng A* 835:142695. <https://doi.org/10.1016/j.msea.2022.142695>
- [46] Zhang L, Harrison W, Yar MA et al (2021) The development of miniature tensile specimens with non-standard aspect and slimness ratios for rapid alloy prototyping processes. *J Mater Res Technol* 15:1830–1843. <https://doi.org/10.1016/j.jmrt.2021.09.029>
- [47] ASTM E111–17 (1997) Standard test method for young's modulus, tangent modulus, and chord modulus. 1–7. <https://doi.org/10.1520/E0111-04.2>
- [48] Roberts D, Zhang Y, Charit I, Zhang J (2018) A comparative study of microstructure and high-temperature mechanical properties of 15–5 PH stainless steel processed via additive manufacturing and traditional manufacturing. *Prog Addit Manuf* 3:183–190. <https://doi.org/10.1007/s40964-018-0051-5>
- [49] Jiang D, Gao X, Zhu Y et al (2022) In-situ duplex structure formation and high tensile strength of super duplex stainless steel produced by directed laser deposition. *Mater Sci Eng A* 833:142557. <https://doi.org/10.1016/j.msea.2021>

Publisher's Note Springer Nature remains neutral with regard to jurisdictional claims in published maps and institutional affiliations.

Springer Nature or its licensor (e.g. a society or other partner) holds exclusive rights to this article under a publishing agreement with the author(s) or other rightsholder(s); author self-archiving of the accepted manuscript version of this article is solely governed by the terms of such publishing agreement and applicable law.